AIAA JOURNAL
Vol. 59, No. 10, October 2021

Hysteresis of Shock Train Movement in the Isolator with a Ramp

Tinglong Huang,* Qifan Zhang,† and Lianjie Yue‡
State Key Laboratory of High Temperature Gas Dynamics, Institute of Mechanics, Chinese Academy of Sciences, 100190 Beijing, People's Republic of China
Peng Zhang§
Hong Kong Polytechnic University, Hung Hom, Kowloon, Hong Kong, People's Republic of China
and
Qingjun Zhao¶
Institute of Engineering Thermophysics, Chinese Academy of Sciences, 100190 Beijing, People's Republic of China

https://doi.org/10.2514/1.J060051

Inside the dual-mode scramjet engine, the shock train will move to a new location when the backpressure changes. Few works focus on the response of the shock train position to the backpressure cyclic variation. This work aims to investigate the behavior of the shock train under such backpressure conditions. Experiments were carried out in a Mach 3 direct-connect facility. The isolator is equipped with a ramp that is used to improve the isolator performance. The static pressures along the wall centerlines were measured. The schlieren imaging was used to provide flow visualization. The results show that a significant hysteresis occurs in the shock train position during the backpressure cyclic variation process. It is found that a large-scale subsonic wake flow region forms behind the ramp when the shock train reaches the ramp trailing edge. The capability of the ramp to retain the existence of the wake flow determines the occurrence of the hysteresis. The effects of the ramp height and width on the hysteresis were examined. Based on the experimental data, the oscillation characteristics were discussed by using wavelet analysis and cross-spectrum analysis. The coupled oscillation between the shock train oscillation and the backpressure oscillation was observed.

Nomenclature

A	=	area, m^2
B_i	=	number of pressure ports, where $i = 1, 2, 3 \ldots$
Co	=	coherence
c	=	sound speed, m/s
f	=	frequency, Hz
H	=	isolator height; 40 mm
h	=	ramp height, mm
L	=	distance
Ma	=	Mach number
P	=	total pressure, Pa
p	=	static pressure, Pa
p'	=	fluctuating static pressure, Pa
T	=	temperature, K
TR	=	throttling ratio
t	=	time, s
V	=	propagation speed of the pressure perturbation
W	=	isolator width; 80 mm
w	=	ramp width
x	=	streamwise coordinate. mm
Δ	=	difference between two values
δ	=	boundary layer thickness; 5.4 mm
θ	=	ramp angle
τ	=	time delay, ms
$\uparrow$	=	the direction of increasing throttling ratio
$\downarrow$	=	the direction of decreasing throttling ratio

Subscripts

c	=	critical state
p	=	outlet area with plug
t	=	outlet area without plug
0	=	total or stagnation state
$+$	=	downstream propagation
$-$	=	upstream propagation

I. Introduction

IN A scramjet engine, the isolator section locates between the lower-pressure inlet and the higher-pressure combustor and plays a crucial role in matching different combustion modes of the combustor. The combustion process creates a backpressure environment to cause the formation of multiple coupled shock waves, which is often called a shock train [1,2]. The shock train decelerates the airflow and increases static pressure, thereby supplying suitable airflow to the combustor. If the backpressure is varied, the shock train moves to a new location for pressure balance. Controlling the shock train is very important because a large upstream movement of the shock train may cause an undesired inlet unstart, which results in substantial engine thrust loss and even combustor flameout. Therefore, many methods are developed to detect the leading shock, and thereby the location of the shock train in the isolator [3–5]. The shock train properties are needed to study to ensure sufficient flow to the combustor and to avoid unstart. Matsuo et al. [1] and Gnani et al. [2] reviewed numerous previous studies.

Understanding the flow mechanism of the shock train propagation is important for better understanding the dynamics of inlet unstart. In a real inlet/isolator configuration of the hypersonic flight vehicle, the shock train encounters complex incoming flow conditions,

Presented as Paper 2017-2436 at the 21st AIAA International Space Planes and Hypersonics Technologies Conference, Xiamen, People's Republic of China, March 6–9, 2017; received 10 August 2020; revision received 22 February 2021; accepted for publication 23 February 2021; published online 21 April 2021.

*Postdoctoral Researcher; currently Institute of Engineering Thermophysics, No. 11 Beisihuanxi Road, Chinese Academy of Sciences, 100190 Beijing, People's Republic of China.

†Research Assistant, Institute of Mechanics, Chinese Academy of Sciences, 100190 Beijing, People's Republic of China.

‡Professor, Institute of Mechanics; also School of Engineering Science, University of the Chinese Academy of Sciences, Chinese Academy of Sciences, No.19(A) Yuquan Road, 100049 Beijing, People's Republic of China; yuelj@imech.ac.cn (Corresponding Author).

§Associate Professor, Department of Mechanical Engineering. Senior Member AIAA.

¶Professor, Institute of Engineering Thermophysics; also School of Aeronautics and Astronautics, University of Chinese Academy of Sciences, Chinese Academy of Sciences, 100049 Beijing, People's Republic of China.

for example, a complex background-shock system generated by the inlet compression surface. Tan et al. [6] showed that due to its interaction with the background shocks, the shock train moves upstream unsteadily and slowly when passing the position where the background shocks impinge on the wall. Wagner et al. [7,8] studied the behavior of the upstream-moving shock train by raising a flap at the exit plane of the isolator to increase the backpressure. They found that upstream propagation of the shock train was seen to be highly associated with background-shock-induced separation. Xu et al. [9] and Li et al. [4,10] analyzed the rapid movement of a shock train when it passed the background-shock impingement point on the wall. They confirmed that the shock train movement is closely related to the wall-pressure gradient distributions.

Effective flow control devices (such as the swept ramp [11], micro-ramp [12,13], vortex generator [14,15], and bleeding [16,17]) may be used to prevent or delay the inlet unstart and to improve the performance of the isolator. These devices also can generate shocks and expansion waves that would propagate into the isolator. These background waves can distort the shock train structures [6] and determine the motion path of the upstream moving shock train [6,18]. Chang et al. [19] outlined the research progress on the flow control of the inlet and isolator. Lin et al. [11] and Cao and Zhang [20] used a swept ramp to improve isolator performance and to shorten the isolator length. Lin et al. [11] observed that at increasing backpressure, once the shock train reaches the trailing edge of the ramp, a wake flow region forms and the shock train has only one oblique leading shock originating from the ramp tip. This leading shock stays attached to the ramp trailing edge until the backpressure reaches the unstart limit, causing a sudden upstream movement of the shock train. Cao and Zhang [20] also observed that an optimized ramp can shorten the shock train length and improve the performance of the isolator to resist the backpressure. In their experiments at a Mach number of 1.98, the isolator with an optimized ramp was 12% shorter than that without a ramp.

The preceding discussion shows that substantial research has been performed to investigate the behavior of the shock train at increasing backpressure conditions. For the situation after flow control failure, the majority of the past studies focused on the inlet unstart/restart dynamics [21–23], whereas few studies paid attention to the response of a shock train at an upstream location (without causing inlet unstart) to the backpressure reduction. That is, the behavior of the shock train movement during a cyclic variation process of backpressure is seldom studied. Combustion experiments [24,25] observed that combustion hysteresis occurs in the ramjet/scramjet mode transition when the fuel equivalence ratio changes cyclically. However, these studies are mainly focused on the effect of combustion and did not analyze the shock train movement. The reason for combustion hysteresis is not clear. Huang et al. [26] found in a numerical study that hysteresis in the shock train position occurs during the backpressure cyclic variation process. They observed that once the shock train moves upstream and interacts with the background shocks, it may recede downstream along a different trajectory. However, the mechanism of the hysteresis remains unclear. A detailed investigation is needed to better understand the hysteresis. Therefore, the first objective of this paper is to confirm whether a simple geometry for improving isolator performance can cause hysteresis in the shock train position. The second objective is to investigate the effect of the geometric configuration on the hysteresis. A better understanding of the flow structure in a realistic system with a flow control device could aid in the detection of shock train location. A better understanding of the overall shock train physics can be developed.

II. Experimental Setup

A. Test Facility

The current experiments were conducted in a Mach 3.0 blowdown-type wind tunnel at the Institute of Mechanics of the Chinese Academy of Sciences. The schematic design of the test facility is shown in Fig. 1. The test facility consists of a plenum, a modular two-dimensional nozzle, a constant area isolator, and a downstream part. The plenum is used to stabilize the total pressure of the airflow. The nominal Mach number of 3.0 was selected, and the corresponding nozzle was installed in the wind tunnel. The area of the rectangular exit of the nozzle is 40×80 mm^2. The isolator with a constant area is 40 mm in height H, 80 mm in width W, and 470 mm in length. The x direction is oriented streamwise with the origin ($x = 0$ mm) at the nozzle exit. An optical window in the sidewalls has a length of 230 mm and a height of 40 mm. The downstream part has a length of 390 mm. To choke the exit flow and to vary the isolator backpressure, and thereby change the shock train location, a cone plug is installed at the downstream part of the duct exit to form a geometrical throat. The plug moves along the axial direction. When the exit area for airflow is reduced, the backpressure increases, and vice versa.

B. Diagnostic Techniques and Instrumentation

High-speed wall static pressure measurements are used to study the pressure fluctuations induced by the shock train flow. The measurement data are collected with high-sensitivity absolute pressure transducers. Ten pressure transducers are installed at the bottom wall of the isolator: one is placed in the downstream part (B11), and four sensors are placed in the ring direction of the B12 position in Fig. 1. Due to improper operation, the transducer at port B4 was broken in some tests; and in other tests, the transducer at port B10 was broken. Thus, only nine data points are obtained in each test. The pressure transducers have a pressure range of 500 kPa and a diaphragm resonance frequency of approximately 50 kHz in a cylindrical housing with a diameter of 2.0 mm. The pressure sensors have a quoted comprehensive accuracy of $\pm 0.025\%$ of the full-scale range. A stainless-steel tube (inner diameter of 1.6 mm, and 20 mm long) is used to connect the pressure transducer and the pressure tap. The pressure tap diameter is 0.8 mm on the flow side of the isolator wall, and its length is about 3 mm. Consequently, for the current flow conditions, the cutoff frequency is about 2.4 kHz (Helmholtz resonance frequency). In current experiments, the pressure is sampled at 3.9 kHz.

A conventional Z-type schlieren setup with a vertical knife edge is used to visualize the flowfield. The images are recorded with a Basler acA1920-155um camera at a rate of 100 Hz with an exposure time of 34 μs. The camera field of view covers 50 mm in height and 240 mm in length. The image size is 900×180 pixels, and the image resolution is approximately 4 pixels/mm.

A linear position sensor is used to record the position of the plug in the axial direction. The throttling ratio TR is introduced to quantify the backpressure instead of a measured pressure value because the downstream part is too short. Therefore, the pressure values at port B12 cannot be reliably used as backpressure. The throttling ratio is defined by $TR = 1 - (A_p/A_t)$, where A_p is the actual throat area with

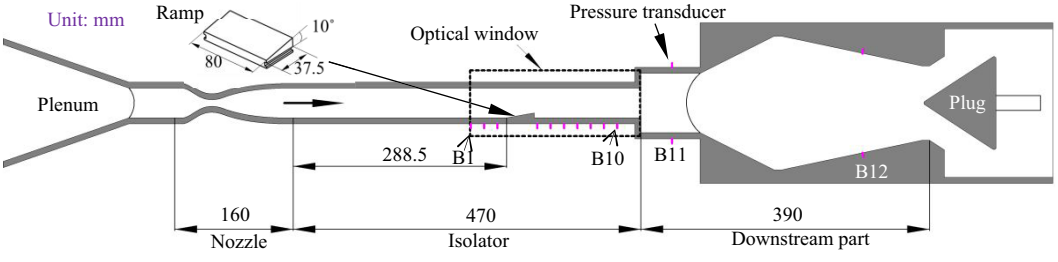

Fig. 1 Schematic of the test facility. Transducer locations are labeled B1 to B12.

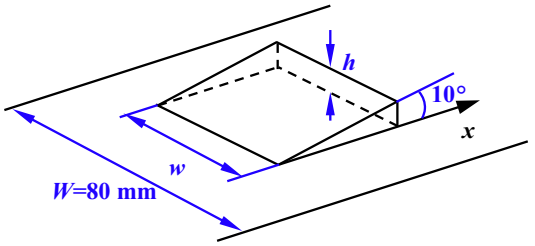

Fig. 2 Schematics for ramp model.

a plug, and A_t is the maximum area without a plug. By moving the plug upstream, the TR is increased and leads to an increase in backpressure. The plug position has a measuring accuracy of ± 0.02 mm. When the plug moves at a speed less than or equal to 30 mm/s, the reported TR has an uncertainty of approximately ± 0.02 with a 95.4% confidence interval for the present test conditions.

C. Ramp Model and Experimental Conditions

The ramp geometry configurations are shown in Fig. 2. The size refers to the configurations of fuel injectors and flow control devices [24,25]. The ramp is installed on the bottom wall. The ramp angle θ is fixed to be 10 deg. A full ramp has the same width w as the isolator width W. The partial ramps are symmetric about the central plane, and their width is smaller than W. The ramp height h of 6.61 mm is selected as the baseline height in the present study. All these ramps are mainly installed at a position of 288.5 mm from the isolator entrance. Additional tests are conducted to estimate the effect of the ramp installation position and to visualize more downstream flow structures. For these tests, the baseline ramp is used and installed at a position of 130 mm from the isolator entrance.

For the present study, the Mach 3.0 airflow is selected as the incoming flow condition, and the total temperature and total pressure inside the plenum are set at $T_0 = 298$ K and $P_0 = 0.93$ MPa, respectively.

III. Results and Discussions

The flowfield inside the isolator with the baseline full ramp was investigated first. The throttling ratio TR is increased (↑) and decreased (↓) stepwise, keeping the backpressure constant at each test point for a certain period. The variation of the TR with time is shown in Fig. 3. After the wind tunnel starts, the plug stays at a location with $TR = 0.430$ where the shock train forms downstream of the ramp. Then, the TR is increased stepwise to the highest value of 0.579, and then it is decreased again in the same steps. When the TR increases, the backpressure increases too.

Instantaneous schlieren images showing the flow structures at constant $TR = 0.430$ (TR increasing phase) and the corresponding time-averaged wall-pressure distribution along with their instantaneous fluctuation range are shown in Fig. 4. The pressure level on the ramp surface is calculated by the oblique shock relations and the averaged pressure measured at ports B1 ~ B2 because no transduces are installed on this surface. As can be seen, the shock train position changes significantly with time. At $t = t0$, the shock train is in the most downstream position captured by the camera. At this moment, the full ramp generates a strong background shock (named the ramp shock hereinafter) that impinges on the top wall and induces shock-wave/boundary-layer interaction. Thus, the separation bubble, the separation shock, and a reattachment shock associated with the separation bubble can be seen in the image. Both shocks impinge on the lower wall at a downstream position. Due to the sudden expansion at the trailing edge of the ramp, a typical backward-facing step flow pattern forms, consisting of the expansion fan, a small separation zone, and a reattachment shock behind the ramp. The lowest static pressure is measured at port B4 ($x = 330$ mm) in the separation zone. At this moment, only the upper leading shock can be seen and the bottom leading shock is outside of the schlieren image. At $t = t1$, due to the backpressure perturbation, the shock train moves to the most upstream position. The bottom leading edge of the shock train is upstream of the bottom wall impingement points. The analysis of the unsteady behavior will be addressed later.

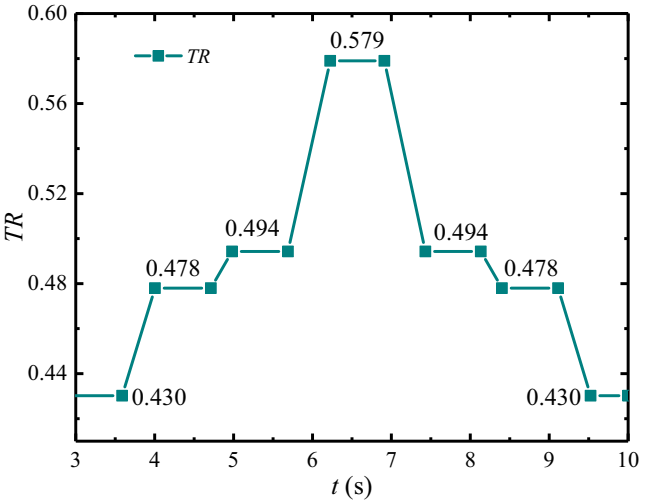

Fig. 3 The histories of the throttling ratio during a test with the full ramp inside the isolator.

A. Flowfield Hysteresis Occurring in the Shock Train Movement

The shock train structure and its response to backpressure variation and the corresponding wall-pressure distributions are shown in Fig. 5. Since the flowfield is highly oscillatory at some TR conditions, schlieren images of the transient flowfield are selected in consistency with the trend of backpressure change. The unsteady flowfield characteristics at these TR conditions will be discussed in the next subsection.

Figures 5a–5d correspond to the increasing phase of the TR, and Figs. 5e–5h correspond to the decreasing phase. For $0.430 \leq TR \leq 0.494\uparrow$, from the perspective of time averaging, the shock train moves slightly forward. The bottom leading shock of the shock train fluctuates around the impingement point of the separation shock. Overall, the flowfields at this TR range seem similar to those in Fig. 4. The difference in flowfields is the farthest position that the shock train can reach. Because the TR is further increased from 0.494 to 0.579, the shock train reaches the ramp trailing edge. Then, the bottom leading shock of the shock train is anchored at the ramp trailing edge, and a free shear layer forms at the tip of the ramp as shown in Fig. 5d. A large-scale separation zone, named the wake flow region, forms downstream of the ramp. Meanwhile, the expansion fan is replaced by a trailing shock at some moment due to the pressure rise in the wake flow region. The pressure profiles at $TR = 0.579$ show that the time-averaged static pressure behind the ramp is greater than that calculated for the ramp surface. At $t = t1$ (Fig. 5d), a large-scale separation bubble (LSB) is visible on the top wall, and the trailing shock seems to coincide with the bottom leading shock of the shock train; whereas the trailing shock disappears at $t = t2$ (Fig. 2e) and the shock train does not seem to be visible in the schlieren field of view. Besides, the flowfield is divided into two parts by the shear layer, with the upper part being the supersonic core flow and the bottom part being the subsonic wake flow.

As the TR is decreased from 0.579 to 0.430, the backpressure is decreased. At $TR = 0.494\downarrow$ and $0.478\downarrow$, there is still no shock train structure visible in the flowfield, as indicated by Figs. 5f and 5g. However, the flowfield structures are almost unchanged, and the oscillation seems to be very weak. Interestingly, the subsonic bottom wake flow region still exists behind the ramp and the static pressure behind the ramp step remains at a high level. The backpressure can propagate to the ramp trailing edge by passing through the subsonic wake flow region. The separation shock and the reattachment shock hit on the outer edge of the wake flow region. Then, a reflected shock propagates downstream. As the TR is further decreased from 0.478 to 0.430, the wake flow region has disappeared.

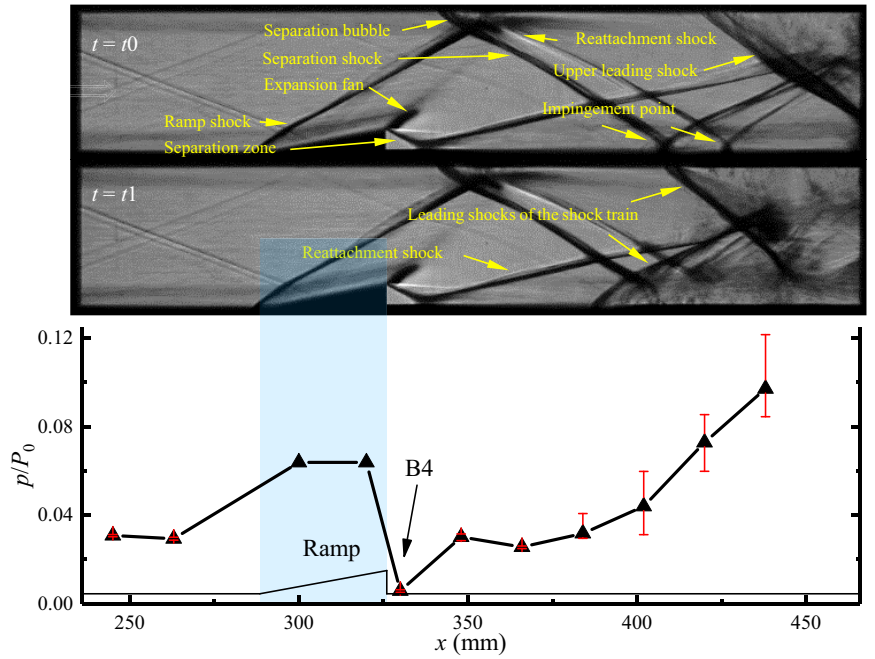

Fig. 4 Instantaneous schlieren images and time-averaged wall-pressure distribution with the fluctuation range at $TR = 0.430$ (pressure value on ramp surface calculated by oblique shock relations).

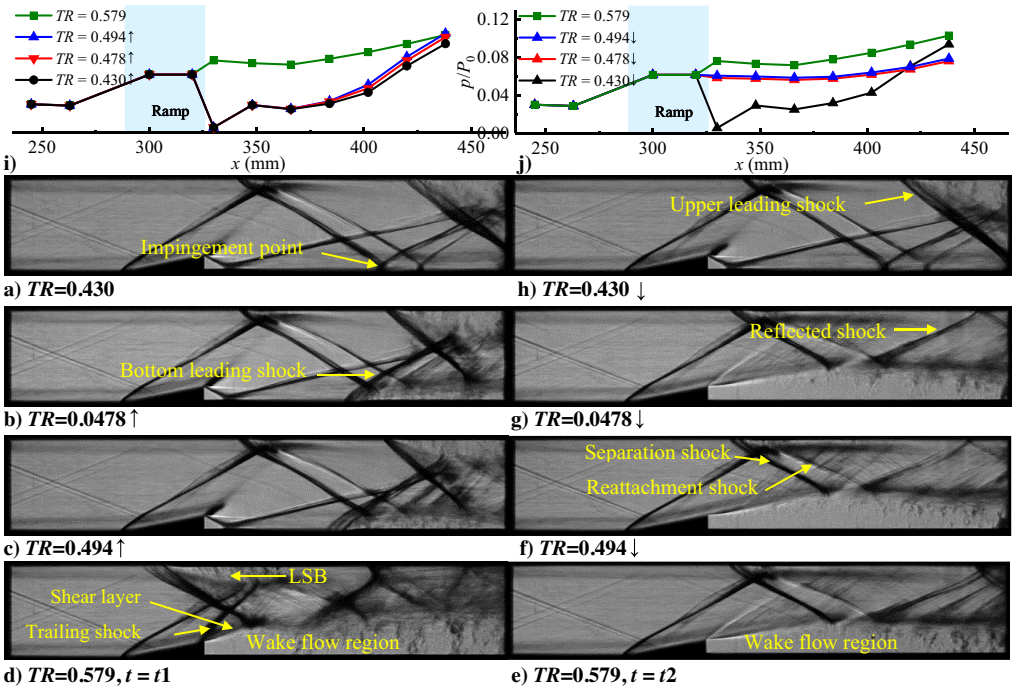

Fig. 5 Schlieren images and the corresponding time-averaged wall-pressure distributions at different TR.

By comparing the flowfield structure in the shown images and the wall-pressure distributions at the same TR condition, it can be found that a hysteresis phenomenon occurs in the shock train movement during the cyclic variation process of backpressure. The flow structure inside the isolator depends not only on the TR condition but also on whether the TR is increasing or decreasing.

Based on the aforementioned analysis, it can be found that the wake flow plays an important role in causing hysteresis because it appears and disappears at different TR conditions. To more closely examine the flow structure inside the subsonic wake region, the experiment was repeated after adjusting the shading of the knife edge of the schlieren imaging device. Figure 6 shows the flow structure within the wake flow region at $TR = 0.494 \downarrow$ and 0.579. Based on the density gradient distribution, it can be seen that the wake flow region consists of a shear layer and a separation zone behind the ramp step. The shear layer originates from the tip of the ramp, then fully develops, and finally seems to attach to the bottom wall. The separation shock impinges on the shear layer and then reflects. The impingement point becomes the highest point of the shear layer. Limited by the technique of schlieren imaging, the three-dimensional structure of the separation zone and the shear layer are not obtained. But, Fig. 6 clearly shows the vortical flow structure of the flowfield in the wake flow region. The spanwise structures of the vortical flow may be very complicated.

Since the shock train is not visible at $TR = 0.494 \downarrow$ and $0.478 \downarrow$, an additional experiment was performed to investigate the flow structure downstream of the wake flow region by moving the full ramp upstream to a new location of $x = 130$ mm. With the TR test points adapted

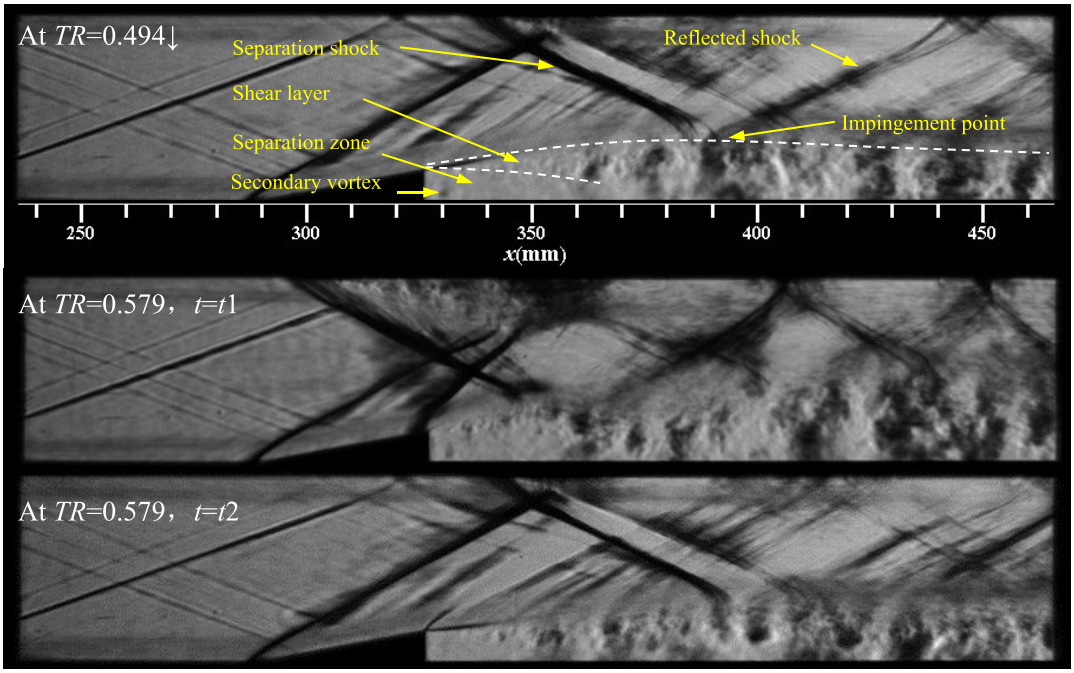

Fig. 6 Vortical flow structures within the wake flow region at different TR conditions.

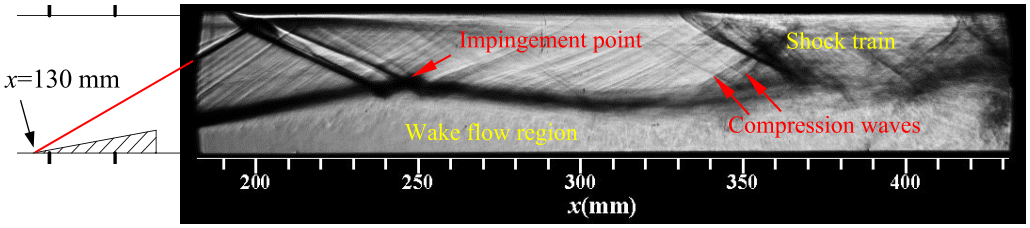

Fig. 7 Flowfield downstream of the wake flow region at $TR = 0.668\downarrow$.

adequately, a comparable hysteresis to that in Fig. 5 is observed. Figure 7 presents a schlieren image of the wake flow region and its downstream flowfield for a decreasing TR (↓) when the wake flow region is about to disappear. It can be found that the shock train forms downstream of the wake flow region. That is, the leading edge of the shock train locates downstream of the wake flow region instead at the ramp trailing edge. This is assumed to be the reason why there is no shock train visible in the flowfield in Figs. 5e–5g. Unusually, the bottom leading shock consists of not a single shock originating from the bottom wall but of converging compression waves originating from the edge of the wake flow region. The subsonic wake flow "bridges" the ramp and the shock train. Consequently, the backpressure can propagate upstream to the ramp through the subsonic flow region. If the backpressure increases slightly at this moment, the shock train would suddenly move upstream and the flowfield (similar to Fig. 5d) would form with the shock train anchoring at the ramp trailing edge. The shock train seems to cross the impingement point and suddenly reach the ramp trailing edge. This demonstrates that the long, narrow subsonic wake flow region plays a crucial role in causing the hysteresis in the shock train movement.

B. Unsteadiness of Flowfield During the Shock Train Movement

The shock train is an inherently unsteady system. For the shock train inside a constant section area isolator under the uniform inflow condition, it is called self-excited oscillation [1]. In this subsection, the oscillation characteristics of the flowfield mentioned before are presented.

Figure 8 presents the wavelet analysis results of the fluctuating static pressure signal p' of port B10 (marked in Fig. 9). Port B10 is the most downstream measurement point on the bottom wall and experiences all flow oscillations throughout the full test period. The p' is the fluctuation relative to the average pressure calculated by the 1000-order one-dimensional median filter. The continuous wavelet transform is performed with the Morlet method, with the wave number being set as 20.

As indicated by the wavelet analysis results, at $0.430 \le TR \le 0.494\uparrow$, the flowfield oscillates with a dominant frequency between 320 and 360 Hz. The dominant frequency becomes slightly higher as backpressure increases. At $0.494\uparrow < TR < 0.548\uparrow$, the dominant frequency gets unspecific. At $t = 6.022$ s ($TR = 0.548\uparrow$), the shock train reaches the ramp trailing edge and another strong oscillation stage begins. The majority of the power is confined to a frequency around 252 Hz. When the backpressure is slightly decreased from 0.579, this strong oscillation disappears at $TR = 0.534\downarrow$ ($t = 7.184$ s). Subsequently, the flowfield enters the hysteresis stage where no dominant frequency is observed until the wake flow region disappears at $TR = 0.446\downarrow$ ($t = 9.390$ s), when the backpressure is sufficiently low. Now, the dominant oscillation frequency is again 320 Hz.

At $0.430 \le TR < 0.494\uparrow$, the flowfield oscillations are comparable. Thus, only the instantaneous flow structures of the shock train at $TR = 0.494\uparrow$ are further analyzed and presented in Fig. 9. These images demonstrate the transient process that belongs to Fig. 5c. As can be seen, the bottom leading shock of the shock train oscillates around the impingement point on the bottom wall. For a uniform incoming flow, the time-averaged position of oscillating leading shocks of a shock train is only determined by backpressure [1,27]. Under the condition of background shocks, the leading shocks would fluctuate around the impingement point of these shock waves as if the shock train were "trapped" by the adverse pressure gradient generated by these shocks [9,10]. The dominant frequency is 358.6 Hz at this TR condition (0.494↑). Therefore, the schlieren images recorded at 100 Hz

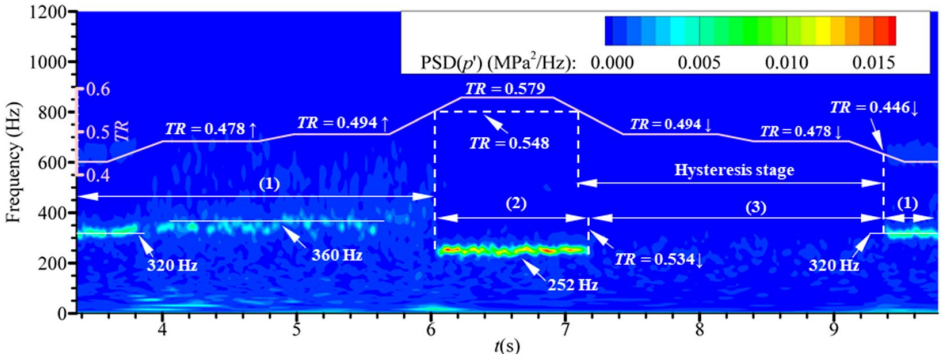

(1) Strong oscillation stage 1; (2) Strong oscillation stage 2; (3) Weak oscillation stage.

Fig. 8 Wavelet analysis of the fluctuation pressure at port B10 during the full test period. The color represents the mean-squared amplitude of the power spectral density (PSD = power spectral density).

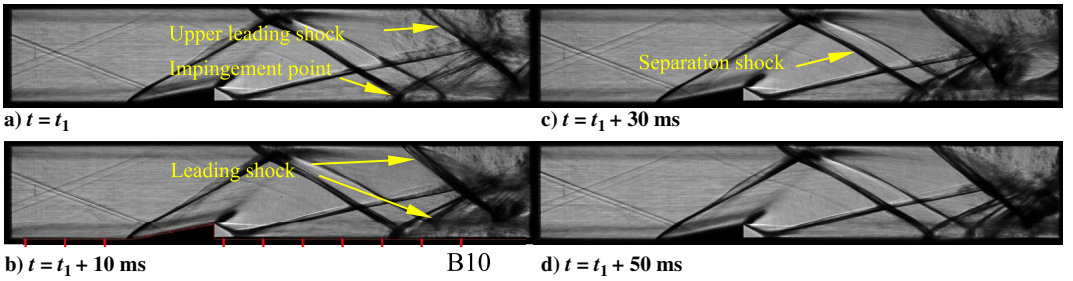

Fig. 9 Instantaneous schlieren images to demonstrate the fluctuation of the bottom leading shock around the impingement point of the background shocks at $TR = 0.494\uparrow$.

cannot be used for a deeper analysis of the oscillation. Figure 10 presents the cross-spectrum results of the pressure signals at ports B10 and B12. The cross-spectrum analysis provides a frequency-dependent evaluation of the correlation between two time-varying signals. Coherence (denoted by Co hereinafter) describes the correlation between these two signals. The time delay (denoted by τ hereinafter) can be used to determine which signal fluctuates first. The results show that for the dominant frequency 358.6 Hz, $Co = 0.57$ and $\tau = 0.99$ ms, indicating that port B12 fluctuates before port B10 and that the source of the shock train oscillation is the backpressure oscillation. However, the backpressure oscillation is not inherent in the system but is coupled with the oscillation of the leading shock around the impingement point. This coupled oscillation is established

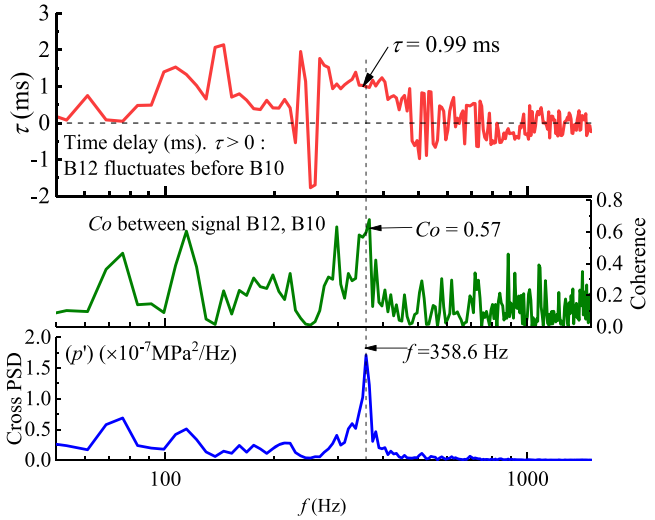

Fig. 10 B12 and B10 cross-spectrum results of time delay, coherence, and cross-power spectral density (cross spectrum computed using Welch averaging method with a Hanning window and 50% overlap; spectrum resolution is 7.6 Hz).

between the outlet plane (the exit of the downstream part) and the impingement point of the background shock. The dominant frequency can be estimated by $f = \overline{c}(1 - \overline{Ma}^2)/2L$ [28,29], where $\overline{c}$ is the average sound speed, $\overline{Ma}$ is the average Mach number, and L is the distance between the impingement point and the outlet plane. In the current experiments where $\overline{Ma}$ is about 0.1, $\overline{c}$ is about 330 m/s, and L is about 0.43 m, the estimated frequency is 380 Hz and only slightly higher than the measurement value. In addition, the frequency estimation equation predicts that the frequency increases with decreasing $\overline{Ma}$, which is consistent with the current experimental results, where the frequency increases from 320 to 360 Hz. As the TR increases, the flow within the downstream part section will decelerate, $\overline{Ma}$ becomes smaller, and the oscillation frequency is higher.

At $0.494\uparrow \leq TR < 0.548\uparrow$, the dominant frequency is indefinite because the shock train can interfere with the separation zone behind the ramp step to change the oscillation characteristics. As shown in Fig. 11, the pressure signal at port B4 shows several spikes in that throttling ratio range. The schlieren image at $t = 5.88$ s indicates that the shock train interferes with the separation zone through the corner flow. But, the backpressure is still too small to anchor the shock train at the ramp trailing edge.

When the wake flow region forms ($0.548\uparrow \leq TR \leq 0.579$), the complete flowfield becomes highly oscillating. The transient flowfield is shown in Fig. 12. The size of the separation bubble on the top wall changes drastically. This is related to the trailing shock, because when this shock disappears, the LSB quickly becomes smaller. Together with the flow structures shown in Fig. 7, it can be seen that the position of the shock train changes significantly. To determine the source and propagation direction of the pressure perturbation, Fig. 13a shows the time delay and coherence of the cross-spectra analysis between the pressure signal at port B4 and that at other ports. It is found that all the coherence coefficients between port B4 and other ports are greater than 0.9 and that the pressure at port B12 starts to fluctuate before the others. Figure 13b presents the pressure time histories at ports B4 ~ B10. The wall-pressure time histories prove that the pressure begins to decrease at port B10 (or even port B12) and the pressure begins to increase at port B5. Thus, this strong oscillation is closely related to the backpressure oscillation. Unusually, the time

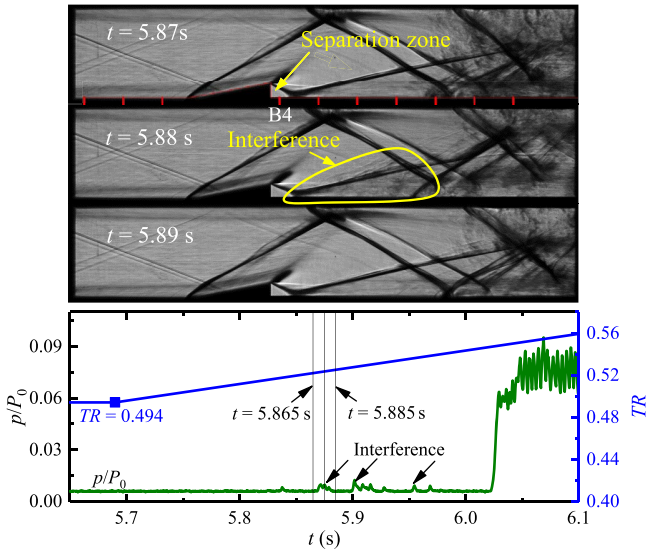

Fig. 11 Pressure signal at port B4 and the corresponding flowfield evolution.

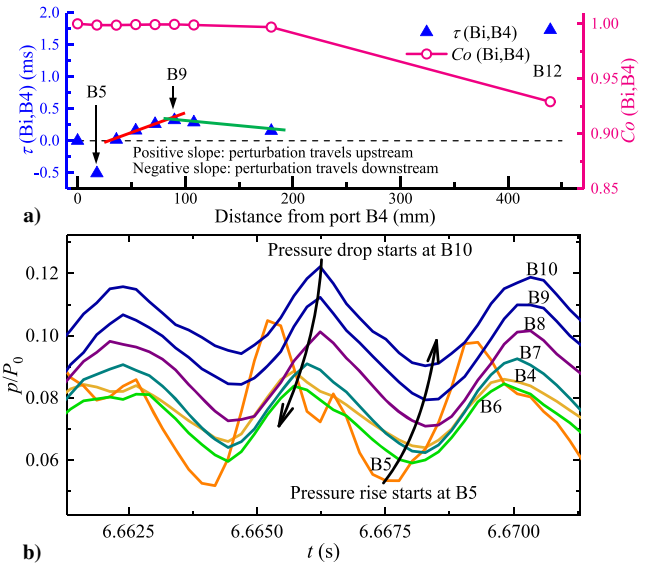

Fig. 13 Representations of a) time delay between pressure signal at port B4 and that at other ports; and b) pressure time histories at ports B4 ~ B10 at $TR = 0.579$.

delay is negative between ports B4 and B5 and at least three times larger than that between two adjacent ports in the region between port B6 and port B11. From the time delay results, the pressure at port B4 fluctuates before port B5. The propagation velocity in the adjacent region behind the ramp is different from that downstream of this region. This is because that the region ahead of port B6 is the separation zone but the downstream of this zone is the reattached shear layer flow, as can be seen in Fig. 6. The speed of the pressure perturbation propagation in the wake flow region can be estimated from the time delay and the distance between two adjacent measuring ports. In the region between ports B6 and B9, the upstream propagation velocity (denoted by V_-) is about -175 m/s, whereas the downstream propagation velocity (denoted by V_+) is about 526 m/s from ports B9 to B11. The propagation distance L between the outlet and the ramp trailing edge is about 0.5 m. Consequently, the dominant frequency can be estimated as $f = 1/(L/V_- + L/V_+) = 263$ Hz, which is very close to the wavelet analysis results (252 Hz).

Based on the preceding analysis, the sequence in Fig. 12 is considered as follows. At some point, the pressure perturbation generated in the exit travels upstream and creates the trailing shock. Then, the LSB appears subsequently. The LSB pushes the separation shock upstream. Consequently, the impingement point of the separation shock on the shear layer moves upstream. This is followed by a pressure drop in the wake flow region. Thus, the trailing shock disappears and is even replaced by an expansion fan. Then, the LSB gets smaller. Once the pressure perturbation arrives again, the trailing shock will be created again, and then the new oscillation period starts. This oscillation is a self-sustaining phenomenon and is not the same as the shock train self-excited one that is usually observed. It is also a coupled oscillation between the shock train position oscillation and the backpressure oscillation.

The preceding analysis indicates that when the hysteresis occurs in the shock train movement inside the isolator with a ramp, it can be detected from the oscillation characteristics of the pressure signal at port B10. This finding could be used to interpret the monitored flow conditions in a real isolator.

C. Effect of Ramp Height and Width on the Hysteresis

To quantify the effect of different ramp configurations on the hysteresis, the critical throttling ratio TR_c at which the wake flow region either appears or disappears is used. An arrow behind represents whether the TR is increasing or decreasing. The $TR_c \uparrow$ reflects the capability of the ramp flow to overcome the backward-facing step without separation, and the $TR_c \downarrow$ reflects the capability of the ramp for holding the wake flow region. The difference ΔTR_c between these two TR_c can be used for quantification of the hysteresis when the inflow conditions are the same among different tests.

To determine the TR_c precisely, the plug moves continuously and slowly at a speed of 6 mm/s to provide sufficient time for the shock train response to the backpressure variation. Since all the pressure signals, the linear position sensor, and the schlieren images are simultaneously sampled, the TR_c can be obtained from the record of the position sensor signal. The existence of the wake flow region mainly depends on the backpressure magnitude. Thus, the TR_c does not depend on whether the plug moves continuously or in intervals.

Figure 14 shows the TR histories of two tests. The original TR signal that samples at 3.9 kHz was subject to strong electromagnetic interference. Thus, it was smoothed by the 1000-order one-dimensional median filter. The smoothed curves of different tests have a good agreement. After determining the time instant when the wake flow appears or disappears, the TR_c can be determined accordingly from the smoothed signal.

Four full ramps with different heights were tested first to study their effect on the hysteresis. Each ramp model was tested at least three times. The ramp height is normalized with the boundary-layer thickness (5.4 mm) not far upstream of the ramp ($x = 240$ mm),

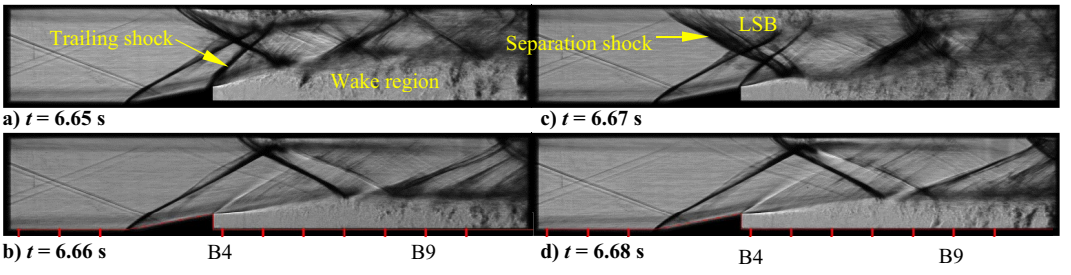

Fig. 12 Instantaneous schlieren images at $TR = 0.579$.

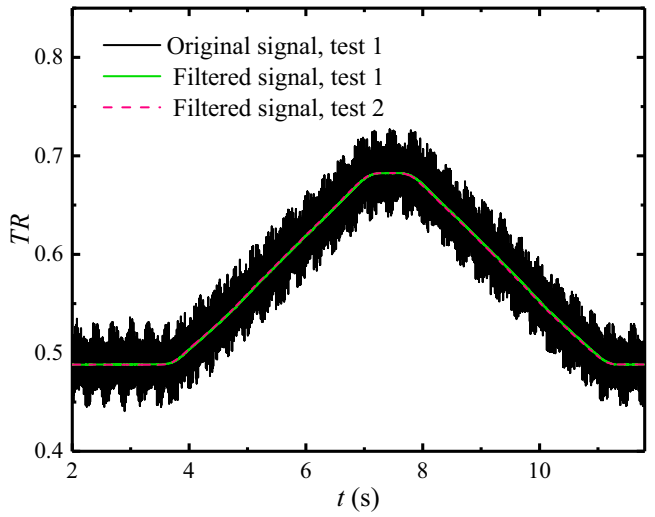

Fig. 14 The original signal and filtered signal of TR collected from two tests.

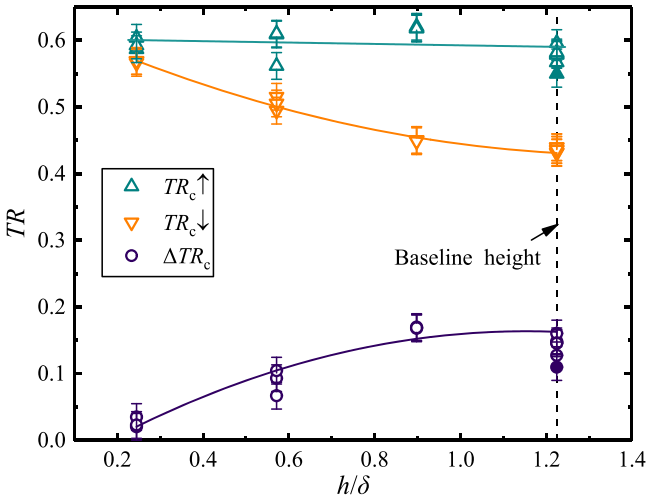

Fig. 15 The critical TR versus the normalized ramp height.

which is determined via pitot probe measurements. Figure 15 shows the change of $TR_c\uparrow$, $TR_c\downarrow$, and ΔTR_c with the normalized ramp height. As indicated by the trendline for ΔTR_c, the hysteresis effect becomes more pronounced as the ramp height increases. The $TR_c\downarrow$ decreases as ramp height increases, whereas the $TR_c\uparrow$ is almost unchanged. Figure 16 presents the time-averaged pressure profiles before the wake flow region either forms (Fig. 16a) or disappears (Fig. 16b). The pressure data are averaged for a period of 10 ms (see schematic in the figure) before the critical point TR_c is reached and used for the critical pressure at each port. The pressure at port B12 is the averaged value of four transducers and can be roughly regarded as the backpressure. Figure 16a indicates that the backpressure levels are almost the same in the cases with different ramp heights. Only the backpressure in the case with $\delta/h = 0.90$ is slightly higher than the others, resulting in a relatively high $TR_c\uparrow$. In the investigated cases, the pressure distributions indicate that the capability of the ramp flow to overcome the backward-facing step without separation is nearly independent of the ramp height. On the other hand, Fig. 16b indicates that the critical backpressure (port B12) decreases with the ramp height, indicating that the capability of holding the wake flow region depends on the ramp height. The difference in this capability leads to the different hysteresis effects.

Eight partial ramps with different widths ($w/W < 1$) were further tested to study their effect on the hysteresis. These partial ramps have a baseline height of $h/\delta = 1.22$. In Fig. 17, the schlieren images in the case with the ramp width of $w/W = 0.5$ are presented to illustrate the shock train structure and its response to the TR variation. The TR is increased stepwise first and then decreased in the same intervals, which are adapted to the current test setup. As expected, this partial ramp also causes hysteresis in the location of the moving shock train. The flowfield shows a very similar evolution process of shock train structures compared to that in Fig. 5. The wake flow still plays a crucial role in causing hysteresis, as shown in Figs. 17d–17i. The difference is that the shock train is always visible at $TR = 0.687$ (Figs. 17d and 17e) and the flowfield is unstable but no specific frequency is found. However, after the TR is decreased to 0.545, the flowfield oscillation similar to that in Figs. 5d and 5e appears as shown in Figs. 17f and 17g. The corresponding dominant frequency is 268 Hz. This coupled oscillation does not appear when the shock train has just reached the ramp trailing edge but when the TR is decreased from a higher level. This phenomenon holds for the cases with $w/W = 0.375 \sim 0.875$. As the TR is further decreased to 0.446 (Figs. 17h and 17i), the flowfield oscillation becomes very weak but the shock train still can reach the ramp trailing edge at some moment due to the weak backpressure perturbation. Overall, although the flowfield is unstable the oscillation intensity is relatively weak for the reduced width from the power spectrum analysis results (not shown here).

Since the partial ramp can introduce significant three-dimensional effects into the flow, the schlieren imaging cannot provide enough information to analyze the complicated flow structures inside the wake region. Therefore, the effect of ramp width on the critical throttling ratio TR_c is mainly discussed rather than the flowfield structure. The corresponding tests are performed with the same continuous TR variation path as that in Fig. 14. The TR_c variation with the ramp width is shown in Fig. 18. The results show a complicated trend, especially for the $TR_c\downarrow$ and ΔTR_c values, probably due to the flow three-dimensionality. Interestingly, the results show that the ΔTR_c slightly increases first, and then it decreases sharply as the ramp width is reduced. When changing the ramp width from $w/W = 0.375$ to 0.25, ΔTR_c drops to zero owing to the increase of $TR_c\downarrow$, which means that the hysteresis disappears. The rapid rise in $TR_c\downarrow$ indicates that the ramp width of $w/W \le 0.25$ is too small to maintain the existence of the wake flow

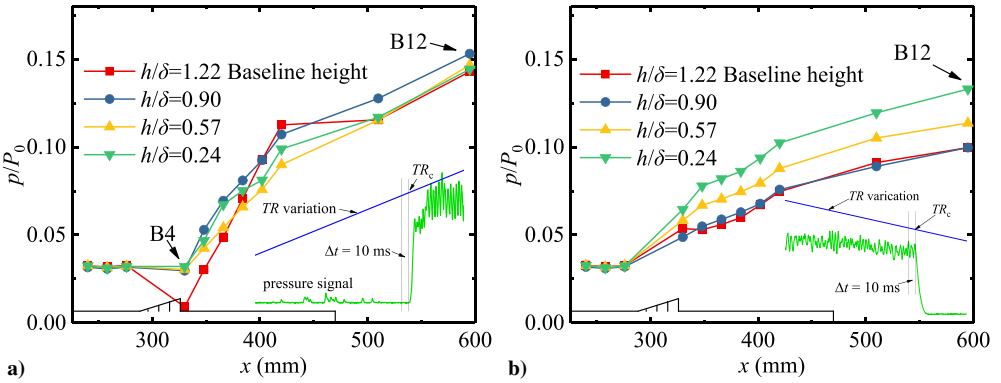

Fig. 16 Critical time-averaged wall-pressure profiles at centerline and method for averaging pressure a) at slightly smaller than $TR_c\uparrow$, and b) at TR slightly larger than $TR_c\downarrow$. Time width for averaging data is 10 ms.

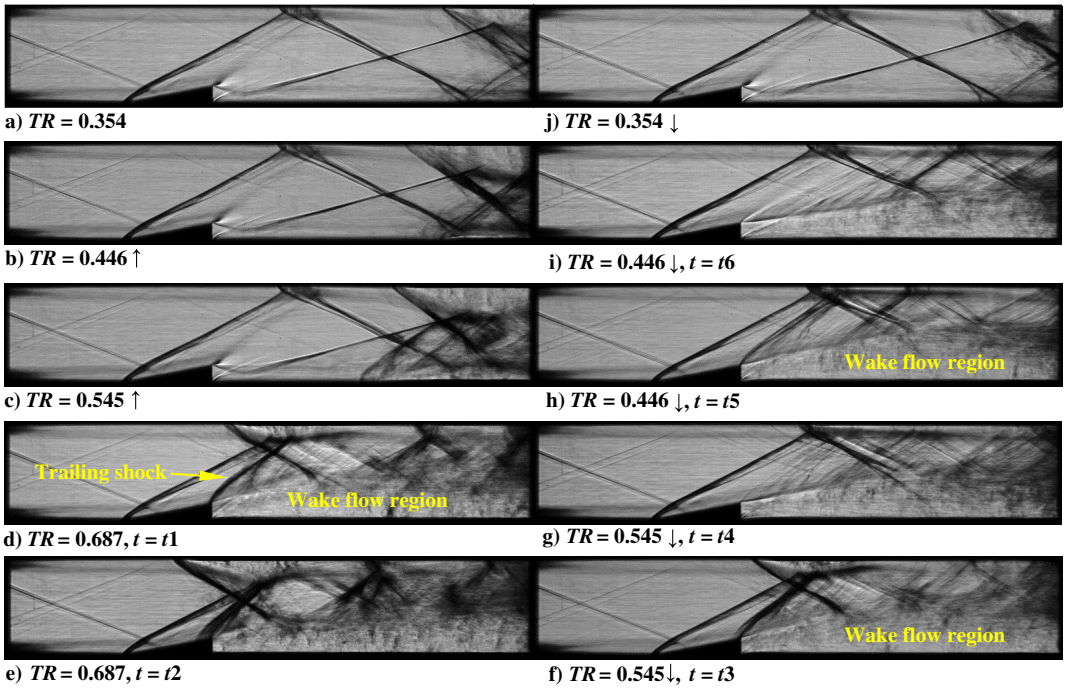

Fig. 17 Schlieren images to illustrate the shock train structures during a cyclic variation process of TR for the case with a ramp width of $w/W = 0.5$.

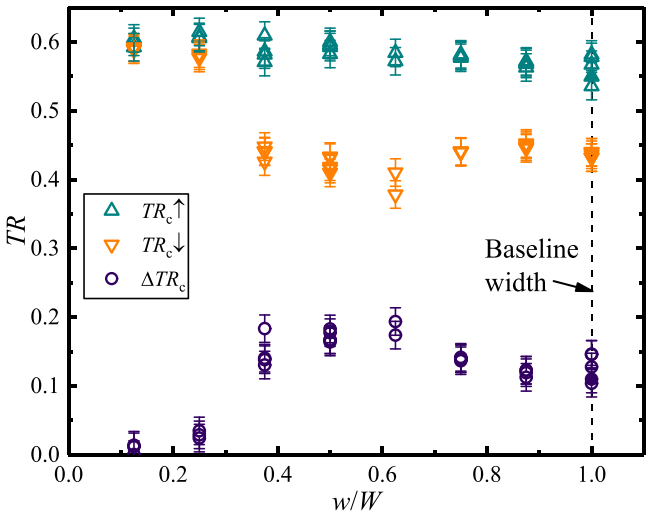

Fig. 18 The critical TR versus the normalized ramp width.

region to cause hysteresis. On the other hand, the TR_c ↑ increases slightly as the ramp width decreases due to the three-dimensional flow effects introduced by the partial ramp. In this situation, the partial ramp serves as a vortex generator and induces streamwise vortices. The vortices contribute to the boundary layer to resist the separation induced by the shock train. Thus, for a smaller ramp width, the wake flow region forms at a higher backpressure (TR_c ↑). This trend continues until a ramp width of $w/W = 0.25$.

From the preceding analysis, it can be concluded that the hysteresis in the shock train position is influenced by the geometric changes of the ramp and that it can be well characterized by the critical throttling ratios at increasing and decreasing backpressures.

IV. Conclusions

Comprehensive experimental tests were conducted in a blowdown direct-connect facility to investigate the shock train movement inside a ramp-equipped isolator at a Mach-number-3.0 inflow condition, with emphasis on the hysteretic response of the shock train position to the backpressure cyclic change. Various ramp configurations used for flow control devices were tested to examine their effect on the hysteresis. A moveable plug was placed in a throat at the duct exit to shift the shock train to various positions. The schlieren imaging was used for flow visualization. Wall static pressures along the centerline on the isolator walls were measured to characterize pressure profiles and oscillation properties. The major conclusions of the present study are as follows:

1) The ramp configurations can readily induce hysteresis in the shock train position during the backpressure cyclic variation process. The occurrence of the wake flow behind the ramp step is the main cause. The capability of holding the wake flow for the ramp determines whether the hysteresis will occur.

2) Decreasing the ramp height can effectively reduce the hysteresis effect but decreasing the ramp width cannot unless the ramp width is sufficiently smaller than the isolator width. Design of the ramp, therefore, is a compromise between effectiveness and the drawback of occurring shock train hysteresis.

3) Due to the hysteresis, the flow oscillation characteristics are different between the increasing phase and the decreasing phase of the backpressure. At the increasing stage, the coupled oscillation phenomenon is observed. At the decreasing stage, no significant oscillation is observed. This finding can be used to interpret the monitored flow state in realistic situations.

Moreover, the present experimental work resulted in an interesting finding that is very important for improving the design of a flow control device. For the partial ramps, it is not generally true that the smaller the width, the weaker the hysteresis. The hysteresis effect will increase if the ramp width is not sufficiently reduced; only if the ramp width is less than a critical value will the hysteresis disappear. Future studies are needed to investigate whether other flow control devices would cause similar hysteresis that could be critical for their application. Besides, the effect of hysteresis on scramjet performance also needs to be evaluated in future studies.

Acknowledgments

This work is funded by the National Natural Science Foundation of China (grant nos.11672309 and 11472279). The work in the Hong

Kong Polytechnic University was supported by a Central Research Grant (G-UAHP and G-YBXN).

References

[1] Matsuo, K., Miyazato, Y., and Kim, H. D., "Shock Train and Pseudo-Shock Phenomena in Internal Gas Flows," *Progress in Aerospace Sciences*, Vol. 35, No. 1, 1999, pp. 33–100. https://doi.org/10.1016/S0376-0421(98)00011-6

[2] Gnani, F., Zare-Behtash, H., and Kontis, K., "Pseudo-Shock Waves and their Interactions in High-Speed Intakes," *Progress in Aerospace Sciences*, Vol. 82, April 2016, pp. 36–56. https://doi.org/10.1016/j.paerosci.2016.02.001

[3] Vanstone, L., Lingren, J., and Clemens, N. T., "Simple Physics-Based Model for the Prediction of Shock-Train Location," *Journal of propulsion Power*, Vol. 34, No. 6, 2018, pp. 1428–1441. https://doi.org/10.2514/1.B37031

[4] Li, N., Chang, J. T., Xu, K. J., Yu, D. R., Bao, W., and Song, Y. P., "Prediction Dynamic Model of Shock Train with Complex Background Waves," *Physics of Fluids*, Vol. 29, No. 11, 2017, Paper 116103. https://doi.org/10.1063/1.5000876

[5] Kong, C., Chang, J., Li, Y., and Li, N., "Flowfield Reconstruction and Shock Train Leading Edge Detection in Scramjet Isolators," *AIAA Journal*, Vol. 58, No. 9, 2020, pp. 4068–4080. https://doi.org/10.2514/1.J059302

[6] Tan, H. J., Sun, S., and Huang, H. X., "Behavior of Shock Trains in a Hypersonic Inlet/Isolator Model with Complex Background Waves," *Experiments in Fluids*, Vol. 53, No. 6, 2012, pp. 1647–1661. https://doi.org/10.1007/s00348-012-1386-1

[7] Wagner, J. L., Yuceil, K. B., Valdivia, A., Clemens, N. T., and Dolling, D. S., "Experimental Investigation of Unstart in an Inlet/Isolator Model in Mach 5 Flow," *AIAA Journal*, Vol. 47, No. 6, 2009, pp. 1528–1542. https://doi.org/10.2514/1.40966

[8] Wagner, J., Yuceil, K., and Clemens, N. T., "Velocimetry Measurements of Unstart of an Inlet-Isolator Model in Mach 5 Flow," *AIAA Journal*, Vol. 48, No. 9, 2010, pp. 1875–1888. https://doi.org/10.2514/1.J050037

[9] Xu, K., Chang, J., Li, N., Zhou, W., and Yu, D., "Experimental Investigation of Mechanism and Limits for Shock Train Rapid Forward Movement," *Experimental Thermal and Fluid Science*, Vol. 98, Nov. 2018, pp. 336–345. https://doi.org/10.1016/j.expthermflusci.2018.06.015

[10] Li, N., Chang, J., Yu, D., Bao, W., and Song, Y., "Mathematical Model of Shock-Train Path with Complex Background Waves," *Journal of Propulsion and Power*, Vol. 33, No. 2, 2016, pp. 1–11. https://doi.org/10.2514/1.B36234

[11] Lin, K., Tam, C., Jackson, K., Kennedy, P., and Behdadnia, R., "Experimental Investigations on Simple Variable Geometry for Improving Scramjet Isolator Performance," *43rd AIAA/ASME/SAE/ASEE Joint Propulsion Conference and Exhibit*, AIAA Paper 2007-5378, 2007. https://doi.org/10.2514/6.2007-5378

[12] Pitt Ford, C., and Babinsky, H., "Micro-Ramp Control for Oblique Shock Wave/Boundary Layer Interactions," *37th AIAA Fluid Dynamics Conference and Exhibit*, AIAA Paper 2007-4115, 2007. https://doi.org/10.2514/6.2007-4115

[13] Valdivia, A., Yuceil, K. B., Wagner, J. L., Clemens, N. T., and Dolling, D. S., "Control of Supersonic Inlet-Isolator Unstart Using Active and Passive Vortex Generators," *AIAA Journal*, Vol. 52, No. 6, 2014, pp. 1207–1218. https://doi.org/10.2514/1.J052214

[14] Panaras, A. G., and Lu, F. K., "Micro-Vortex Generators for Shock Wave/Boundary Layer Interactions," *Progress in Aerospace Sciences*, Vol. 74, April 2015, pp. 16–47. https://doi.org/10.1016/j.paerosci.2014.12.006

[15] Verma, S. B., and Manisankar, C., "Control of Incident Shock-Induced Separation Using Vane-Type Vortex-Generating Devices," *AIAA Journal*, Vol. 56, No. 4, 2018, pp. 1600–1615. https://doi.org/10.2514/1.J056460

[16] Weiss, A., and Olivier, H., "Behaviour of a Shock Train Under the Influence of Boundary-Layer Suction by a Normal Slot," *Experiments in Fluids*, Vol. 52, No. 2, 2012, pp. 273–287. https://doi.org/10.1007/s00348-011-1211-2

[17] Tam, C. J., Eklund, D., Behdadnia, R., and Jackson, T., "Investigation of Boundary Layer Bleed for Improving Scramjet Isolator Performance," *AIAA/CIRA 13th International Space Planes and Hypersonics Systems and Technologies Conference*, AIAA Paper 2005-3286, 2005. https://doi.org/10.2514/6.2005-3286

[18] Reinartz, B. U., Herrmann, C. D., Ballmann, J., and Koschel, W. W., "Aerodynamic Performance Analysis of a Hypersonic Inlet Isolator Using Computation and Experiment," *Journal of Propulsion and Power*, Vol. 19, No. 5, 2012, pp. 1600–1615. https://doi.org/10.2514/2.6177

[19] Chang, J., Li, N., Xu, K., Bao, W., and Yu, D., "Recent Research Progress on Unstart Mechanism, Detection and Control of Hypersonic Inlet," *Progress in Aerospace Sciences*, Vol. 89, Feb. 2017, pp. 1–22. https://doi.org/10.1016/j.paerosci.2016.12.001

[20] Cao, X., and Zhang, K., "Experimental Investigation of the Short Isolator with the Ramp Under Asymmetric Incoming Flow," *46th AIAA/ASME/SAE/ASEE Joint Propulsion Conference and Exhibit*, AIAA Paper 2010-6554, 2010. https://doi.org/10.2514/6.2010-6554

[21] Zhang, Q., Tan, H., Chen, H., Yuan, Y., and Zhang, Y., "Unstart Process of a Rectangular Hypersonic Inlet at Different Mach Numbers," *AIAA Journal*, Vol. 54, No. 12, 2016, pp. 3681–3691. https://doi.org/10.2514/1.J055005

[22] Yue, L., Jia, Y., Xu, X., Zhang, X., and Zhang, P., "Effect of Cowl Shock on Restart Characteristics of Simple Ramp Type Hypersonic Inlets with Thin Boundary Layers," *Aerospace Science and Technology*, Vol. 74, March 2018, pp. 72–80. https://doi.org/10.1016/j.ast.2017.12.018

[23] Laurence, S. J., Karl, S., Martinez Schramm, J., and Hannemann, K., "Transient Fluid-Combustion Phenomena in a Model Scramjet," *Journal of Fluid Mechanics*, Vol. 722, 2013, pp. 85–120. https://doi.org/10.1017/jfm.2013.56

[24] Rockwell, R., Goyne, C. P., Haw, W., Krauss, R. H., McDaniel, J. C., and Trefny, C. J., "Experimental Study of Test-Medium Vitiation Effects on Dual-Mode Scramjet Performance," *Journal of Propulsion and Power*, Vol. 27, No. 5, 2011, pp. 1135–1142. https://doi.org/10.2514/1.B34180

[25] Steva, T. B., Goyne, C. P., Rockwell, R. D., Cresci, D., and Osborne, J. W., "Comparison of a Direct-Connect and Freejet Dual-Mode Scramjet," *Journal of Propulsion and Power*, Vol. 38, No. 6, 2015, pp. 1–13. https://doi.org/10.2514/1.B35221

[26] Huang, T., Yue, L., Ma, S., Zhang, Q., Zhang, P., and Chang, X., "Numerical Investigation on Flow Nonuniformity-Induced Hysteresis in Scramjet Isolator," *Chinese Journal of Aeronautics*, Vol. 33, No. 12, 2020, pp. 3176–3188. https://doi.org/10.1016/j.cja.2020.04.019

[27] Hunt, R. L., and Gamba, M., "On the Origin and Propagation of Perturbations that cause Shock Train Inherent Unsteadiness," *Journal of Fluid Mechanics*, Vol. 861, Feb. 2019, pp. 815–859. https://doi.org/10.1017/jfm.2018.927

[28] Ma, F., Li, J., Yang, V., Lin, K., and Jackson, T., "Thermoacoustic Flow Instability in a Scramjet Combustor," *41st AIAA/ASME/SAE/ASEE Joint Propulsion Conference and Exhibit*, AIAA Paper 2005-3824, 2005. https://doi.org/10.2514/6.2005-3824

[29] Lin, K., Jackson, K., Behdadnia, R., Jackson, T. A., Ma, F., and Yang, V., "Acoustic Characterization of an Ethylene-Fueled Scramjet Combustor with a Cavity Flameholder," *Journal of Propulsion and Power*, Vol. 26, No. 6, 2010, pp. 1161–1170. https://doi.org/10.2514/1.43338

F. Grasso
Associate Editor